Article

Comprehensive Analysis on GPS Carrier Phase under Various Cutoff Elevation Angles and Its Impact on Station Coordinates' Repeatability

Sorin Nistor [1] , **Norbert-Szabolcs Suba** [1] , **Aurelian Stelian Buda** [1,*] , **Kamil Maciuk** [2] and **Ahmed El-Mowafy** [3]

1. Faculty of Construction, Cadastre and Architecture, University of Oradea, 410058 Oradea, Romania; sonistor@uoradea.ro (S.N.); nsuba@uoradea.ro (N.-S.S.)
2. Department of Integrated Geodesy and Cartography, AGH University of Krakow, 30-059 Krakow, Poland; maciuk@agh.edu.pl
3. School of Earth and Planetary Science, Curtin University, Perth 6845, Australia; a.el-mowafy@curtin.edu.au
* Correspondence: aurelianbuda@uoradea.ro

Abstract: When processing the carrier phase, the global navigation satellite system (GNSS) grants the highest precision for geodetic measurements. The analysis centers (ACs) from the International GNSS Service (IGS) provide different data such as precise clock data, precise orbits, reference frame, ionosphere and troposphere data, as well as other geodetic products. Each individual AC has its own strategy for delivering the abovementioned products, with one of the key elements being the cutoff elevation angle. Typically, this angle is arbitrarily chosen using generic values without studying the impact of this choice on the obtained results, in particular when very precise positions are considered. This article addresses this issue. To this end, the article has two key sections, and the first is to evaluate the impact of using the two different cutoff elevation angles that are most widely used: (a) 3 degrees cutoff and (b) 10 degrees cutoff elevation angle. This analysis is completed in two major parts: (i) the analysis of the root mean square (RMS) for the carrier phase and (ii) the analysis of the station position in terms of repeatability. The second key section of the paper is a comprehensive carrier phase analysis conducted by adopting a new approach using a mean of the 25-point average RMS (A-RMS) and the single-point RMS and using an ionosphere-free linear combination. By using the ratio between the 25-point average RMS and the single-point RMS we can define the type of scatter that dominates the phase solution. The analyzed data span a one-year period. The tested GNSS stations belong to the EUREF Permanent Network (EPN) and the International GNSS Service (IGS). These comprise 55 GNSS stations, of which only 23 GNSS stations had more than 95% data availability for the entire year. The RMS and A-RMS are analyzed in conjunction with the precipitable water vapor (PWV), which shows clear signs of temporal correlation. Of the 23 GNSS stations, three stations show an increase of around 50% of the phase RMS when using a $3°$ cutoff elevation angle, and only four stations have a difference of 5% between the phase RMS when using both cutoff elevation angles. When using the A-RMS, there is an average improvement of 37% of the phase scatter for the $10°$ cutoff elevation angle, whereas for the $3°$ cutoff elevation angle, the improvement is around 33%. Based on studying this ratio, four stations indicate that the scatter is dominated by the stronger-than-usual dominance of long-period variations, whereas the others show short-term noise. In terms of station position repeatability, the weighted root mean square (WRMS) is used as an indicator, and the results between the differences of using a $3°$ and $10°$ cutoff elevation angle strategy show a difference of -0.16 mm for the North component, -0.21 mm for the East component and a value of -0.75 mm for the Up component, indicating the importance of using optimal cutoff angles.

Keywords: cutoff elevation angle; GNSS; RMS; time series; carrier phase

1. Introduction

The development of global navigation satellite systems (GNSS) such as GPS, GLONASS, BEIDOU and Galileo, along with regional navigation satellite systems like QZSS and NAVIC provide a much higher number of observations at different elevation angles. Using different cutoff elevation angles, we can eliminate the observations of low elevation angles that contain significant noise and multipath, and longer atmosphere delay, and thus avoid their adverse impact on the final solution. By using an increased cutoff elevation angle, the cone of GNSS observations becomes smaller, hence reducing the number of visible satellites.

The GNSS signal, when propagating through the atmosphere, greatly experiences refractivity variations, which represent a source of uncertainty in precise geodetic positioning, resulting in the degradation of station coordinate repeatability, and accordingly, differences in annual and semi-annual signals extracted from the GNSS time series [1–3]. The impact of the neutral part of the atmosphere is commonly called the tropospheric delay, which represents the slowing down and bending of the GNSS signal. Due to this delay, GNSS signals can be used to determine valuable information on the tropospheric wet delay, which presents the amount of water vapor in the troposphere, thus obtaining the precipitable water vapor (PWV) along the signal path [4,5]. It is crucial to understand that the delay introduced by the troposphere is frequency independent, and thus it cannot be eliminated by the linear combination of the GNSS signals of two frequencies, and it equally affects both the pseudorange and carrier phases [3].

By taking advantage of the lower elevation angles, a stronger geometrical solution can be obtained. One of the estimates that benefits from the low elevation angle is the vertical estimate of a GNSS site, but the downside of these low elevation observations is that they are affected by the elevation-dependent error source, mainly the atmospheric corrections [6]. A relatively low cutoff elevation angle, such as $3°$, can be used to decorrelate the GNSS station height and the troposphere estimates during the processing stage in the design matrix [7,8]. The downside of low elevation angle GNSS observations is that they are more susceptible to the multipath effect, mapping function and phase center variations, thus increasing noise and systematic errors; therefore, rigorous weighting of the phase observations is strongly recommended. Furthermore, refs. [9–11] showed that the GNSS measurements down to a $3°$ cutoff elevation angle can cause a contribution of the atmosphere to the hydrostatic path delay within a margin of a radius of 700 km around the GNSS stations. Another problem is the fact that the GNSS height estimate is also strongly correlated to the receiver clock, and thus the GNSS observations for terrestrial reference frames' (TRF) scale determination become elusive [12].

Precise geodetic applications rely on carrier phase observables, hence different weights must be assigned to GNSS observations, such as higher weights assigned for high precision observations, resulting in a meaningful impact of the estimated parameters. A low elevation satellite can negatively impact the final estimates, due to the higher errors caused by the atmosphere and multipath, generating higher noise and lower signal strength [13]. Thus, the weighting procedure of the observations is related to the elevation angle of the satellites due to a possible strong correlation between the elevation angle and the observation noise [13,14].

Over the last decades, significant research has been conducted towards improving the GNSS stochastic model [15–18]. The findings of these studies concerning the GNSS stochastic properties show that (1) the precision of the observations is dependent on the receiver cutoff elevation angle, although the dependence pattern changes with the type of the receiver and observation type; (2) by using a typical user filtering technique, the time correlation may be introduced, to improve the observation precision, mainly for the code measurements; (3) depending on the technique that is implemented on the receiver for decoding, the cross correlation between the observations types may exist [14]. By analyzing the stochastic model, we can observe not only the observations' precision but also if there is a correlation or not, as well as the strength of the correlation of the final estimates with each other [14].

Chengfa et al. (2011) conducted research on the stochastic modelling of GNSS observation for precise point positioning (PPP) adopting an elevation angle and carrier-to-noise-density ratio (C/N0), and as a consequence they obtained an improvement on position accuracy [19]. Moreover, [20]'s research presented higher position accuracy when using different weights for each GNSS system, whereas [13] used eight different weighting procedures dependent on the elevation angle and the results showed a visible impact on the estimation of the vertical component.

The most widespread scientific software used for GNSS processing, such as GipsyX developed by Jet Propulsion Laboratory (JPL) [21], Positioning And Navigation Data Analyst—PANDA developed at Wuhan University [22], Bernese GPS software version 5.0 and higher developed at the Astronomical Institute of the University of Berne [23] or Gamit/Globk developed by Massachusetts Institute of Technology [24] have implemented different approaches for elevation-dependent stochastic models to weight the data by elevation angle, in order to capture the stochastic uncertainties of the observations. The main purpose of these elevation-dependent models is to reduce the contribution of the low elevation angle observations, due to the fact that typically they have a large error contribution to the parameter estimation. With the help of this advance software, when analyzing the GNSS coordinates time series, it is possible to capture the temporal variability of different physical phenomena, such as deformations in the Earth's crust, geodynamic phenomena providing information related to understanding strain and velocity fields, mass transfer, annual and semi-annual seasonal signals and other likewise phenomena [25–28].

At this moment, there are 12 IGS ACs using different cutoff elevation angles such as (a) 3° cutoff elevation angle—adapted by the Center for Orbit Determination in Europe (CODE) and U.S. Naval Observatory (USNO); (b) 7° cutoff elevation angle—used by Wuhan University (WHU), Geodetic Observatory Pecny (GOP), Helmholtz Centre Potsdam (GFZ) and the Jet Propulsion Laboratory (JPL); and (c) 10° cutoff elevation angle—employed by Natural Resources Canada (EMR), European Space Agency (ESA), Massachusetts Institute of Technology (MIT), National Oceanic and Atmospheric Administration (NOAA) and Scripps Orbit and Permanent Array Center (SOPAC). Only the space geodesy team of the CNES (GRG (GRGS-CNES/CLS) is using a 12 degree cutoff elevation angle in their processing strategy (https://files.igs.org/pub/center/analysis/, accessed on 21 March 2023).

The motivation behind the present research is based on the fact that each individual analysis center (AC) is using different strategies related to the cutoff elevation angle and distinct weighting functions for the low elevation angle measurements. Thus, the research presented in the article investigates the impact on the ionosphere-free linear combination (LC) phase scatter, as well as station position repeatability.

The aim and significance of the article are given as two-fold: (a) adopting a new approach to the carrier phase analysis through using the ratio between the mean of the 25-point average RMS (A-RMS) and the single-point RMS for the ionosphere-free linear combination using two different cutoff elevation angles, namely 3° and 10°; and (b) a comprehensive assessment of the influence of two different cutoff elevation angles, namely 3° and 10° on GNSS station coordinates' repeatability. When using the ratio between the 25-point average RMS and the single-point RMS, the type of scatter that dominates the phase solution can be defined.

2. Data and Methods

The used methodology for GNSS processing pursues the recommendation of different agencies, such as the International GNSS Service (IGS) and EUREF Permanent GPS Network (EPN). During the processing strategy, none of the other parameters were changed except the elevation cutoff angle, and thus the variation of the results will primarily depend on the variation of the cutoff elevation angle. For example, the outcome of the influence of ocean loading will generate the same variations in both cases: 3 degrees and 10 degrees cutoff elevation angle. To estimate the unknowns parameters, the least square (LS) method was

applied and the float ambiguities were fixed using the bootstrapping and decision function method [29].

2.1. Stochastic Modelling

The linear observation equations of GNSS are defined as follows:

$$L = Ax + v$$
$$E(v) = 0$$
$$D(v) = C_L \tag{1}$$

where L is the vector of the observed-minus-computed code and carrier phase values (O-C), A is the design matrix, x is the unknown parameters, v is the residual with the variance–covariance (VC) matrix C_L and $E(.)$ and $D(.)$ are the mathematical operators for expectation and dispersion. Using the least square method (LS), the unknown parameters and accuracy indicator can be obtained, namely,

$$\hat{x} = \left(A^T (C_L)^{-1} A\right)^{-1} A^T (C_L)^{-1} L$$
$$v = L - A\hat{x}$$
$$\hat{\sigma}^2 = \frac{v^T (C_L)^{-1} v}{df} \tag{2}$$

where $\hat{x}$ is the parameter estimate, $\hat{\sigma}$ is the standard deviation and df is the degrees of freedom. If we assume that the functional model and the stochastic model are free from error misspecifications, $\hat{x}$ represents the best linear unbiased estimation (BLUE) of x, with C_x as the corresponding estimated variance covariance matrix, resulting from the law of variance covariance propagation.

It can be observed that the estimation of the unknown parameter x and its related indicator of accuracy is relying on the stochastic model, thus any misspecification included in the stochastic model will generate an uncertain estimation of the unknown parameter. Thus, the stochastic model in the LS procedure has an important role.

In order to assess the reliability of the stochastic model, the Chi-square distribution (χ^2) can be used for testing the hypothesis about the variances and detection of outliers. It can mainly be used to test with certainty if a sample is consistent with a postulated probability density function, which conventionally measures the goodness of fit.

The realistic stochastic model, according to [30–32], can be written as:

$$C_L = \Sigma_C \bigotimes \Sigma_T \bigotimes \Sigma_E \tag{3}$$

where $\bigotimes$ is the Kronecker product, and the matrices Σ_C, Σ_T, Σ_E are defined as:

$$\Sigma_C = \begin{bmatrix} \sigma_{\varphi^1}^2 & \sigma_{\varphi^1 \varphi^2} & \sigma_{\varphi^1 P1} & \sigma_{\varphi^1 P2} \\ \sigma_{\varphi^1 \varphi^2} & \sigma_{\varphi^2}^2 & \sigma_{\varphi^2 P1} & \sigma_{\varphi^2 P2} \\ \sigma_{\varphi^1 P1} & \sigma_{\varphi^2 P1} & \sigma_{P1}^2 & \sigma_{P1 P2} \\ \sigma_{\varphi^1 P2} & \sigma_{\varphi^2 P2} & \sigma_{P1 P2} & \sigma_{P2}^2 \end{bmatrix} \tag{4}$$

and

$$\Sigma_T = \begin{bmatrix} \sigma_{(0)} & \sigma_{(1)} & \cdots & \sigma_{(k-1)} \\ \sigma_{(1)} & \sigma_{(0)} & \cdots & \sigma_{(k-2)} \\ \vdots & \vdots & \ddots & \vdots \\ \sigma_{(k-1)} & \sigma_{(k-2)} & \cdots & \sigma_{(0)} \end{bmatrix} \tag{5}$$

and

$$\Sigma_E = 2 \begin{bmatrix} \sigma^2_{[1]} + \sigma^2_{[2]} & \sigma^2_{[1]} & \cdots & \sigma^2_{[1]} \\ \sigma^2_{[1]} & \sigma^2_{[1]} + \sigma^2_{[3]} & \cdots & \sigma^2_{[1]} \\ \vdots & \vdots & \ddots & \vdots \\ \sigma^2_{[1]} & \sigma^2_{[1]} & \cdots & \sigma^2_{[1]} + \sigma^2_{[k]} \end{bmatrix} \tag{6}$$

The diagonal and off-diagonal elements of the cross-correlation matrix—Σ_C represent the variances, respectively, the covariance between the GNSS observable, consisting of ten VC elements for dual-frequency phase and code observation types; the *k x k* Toeplitz matrix—Σ_T represents the possible temporal correlation matrix of the GNSS observable, assuming that the correlation function is of time difference alone, e.g., $\sigma_{(i,j)} = \sigma_{(\tau)} = \sigma_{(i-j)}$. Finally, Σ_E as the *k x k* matrix characterizes the dependency of the GNSS observable's precision with respect to the elevation of the satellite or the elevation-dependent satellite weight matrix, in which the *k* is the satellite number and satellite #1 is assumed to be the reference satellite.

2.2. Satellite Elevation Angle-Dependent Weighting and Accuracy Assesment

Due to a multitude of factors, which generate systematic errors that may be closely related to the satellite elevation angles and azimuth, such as signal-to-noise ratio, multipath and atmospheric delay, these effects can vary from one observed satellite to another. Consequently, each individual GNSS satellite measurement has a different accuracy. In order to model the variances of the GNSS measurements acquired from different satellites, a function of satellite elevation is used to characterize the variance of the raw GNSS measurements, expressed as:

$$\sigma^2_{\phi^s_r(i)} = a^2 + b^2 * f^2(elev^j_r(i)) \tag{7}$$

where *a* and *b* are constant values, and they are computed based on the actual scatter of the residuals from each station, obtaining different values for each individual GNSS station, and $f^2(elev^j_r(i))$ is the function of the satellite elevation angle at epoch *i*.

The weighted root mean square (WRMS), also known as the repeatability precision, is expressed in short and long terms. They are based on the length of the observation time span. The short-term WRMS, which is computed in multi-sessions, has the ability to reflect the data estimates that are affected by multipath, orbital error, atmospheric delay, etc. Performing multiple sessions of GNSS observations, the short-term WRMS reflects the characteristics of the station positioning in the short term. The equation that defines the short-term WRMS, according to [33], is:

$$WRMS_{short} = \sqrt{\frac{\frac{n}{n-1}\sum_{i=1}^n \frac{(x_i - x)^2}{\sigma_i^2}}{\sum_{i=1}^n \sigma_i^2}} \tag{8}$$

where x_i is the daily solution, σ_i is the standard deviation of x_i, *n* is the number of x_i and *x* is the weighted average value of x_i:

$$x = \frac{\sum_{i=1}^n x_i / \sigma_i^2}{\sum_{i=1}^n 1 / \sigma_i^2} \tag{9}$$

In the case of long-term WRMS, it is computed by applying the optimal linear fitting to the positioning estimate of each period when dealing with multiple observation periods. The WRMS of the long term has the potential to reflect the degree of dispersion in the long term of station positioning, as a result of environmental influences such as non-tectonic movement, seasonal atmospheric signal and orbital long period error. The WRMS in the case of the long-term period is given by:

$$WRMS_{long} = \sqrt{\frac{\frac{n}{n-2}\sum_{i=1}^{n}\frac{(l_i-l_i^m)^2}{\sigma_i^2}}{\sum_{i=1}^{n}\sigma_i^2}} \tag{10}$$

where l_i and σ_i are the daily solutions and its associated standard deviation, n is the number of l_i and l_i^m is the optimal linear fitting value.

2.3. GNSS Data

In order to effectively evaluate the performance of GNSS stations in a relatively short period of time, using one year of data (2020), the GNSS data were analyzed considering the RMS of the carrier phase, as well as station coordinates' repeatability for the North (N), East (E) and Up components. The two analyses were conducted by using two different cutoff elevation angles: (a) 3° and (b) 10°. The analyzed data were derived from GNSS stations from the EUREF Permanent Network (EPN) and from the International GNSS Service (IGS) stations which are located in Europe. The aforementioned data were composed of 55 GNSS stations, from which only 23 GNSS stations had more than 95% of available data for the entire year. The data were processed using Gamit-Globk [24]. The reference frame was IGS2014.

This analysis was conducted in two major parts: (1) the analysis of the RMS for the phase data and (2) the analysis of the station position in terms of repeatability. The processing strategies are presented in Table 1.

We used only the GPS constellation, because it was the only system available in all test stations all of the time.

The weighting functions for the low elevation angle measurements were based on the actual scatter of the residuals from each individual GNSS station. Thus, for data processing we used a phase variance σ^2, which is computed from:

$$\sigma^2 = a^2 + \frac{b^2}{sin^2(\varepsilon)} \tag{11}$$

where a and b are coefficients that are estimated from a least square fit to the scatter of the post-fit phase residuals, and ε is the elevation angle.

In the first stage, the carrier phase, namely the ionosphere-free linear combination, termed the LC or L3, was analyzed. For this analysis, we analyzed the RMS of the LC. Furthermore, in addition to the RMS statistics, to be able to conduct a more comprehensive analysis and to better analyze the behavior of the scatter, the ratio between the mean of the 25-point average RMS (A-RMS) and the single-point RMS for the LC was calculated.

This A-RMS was then used to define the type of scatter that dominates the phase solution. By analyzing the A-RMS and RMS of the scatter of the LC phase, we can observe if it was dominated by different types of variations such as random variation, in which case the above ratio was around 5.0; short-term noise was indicated when we had a ratio between 1.5 and 2.0; and stronger-than-usual dominance of long-period variation when the ratio was near 1.0.

Table 1. Summary of GNSS processing strategies.

Items	Description
Number of stations	55
Sampling interval	30 s
Satellite constellation	GPS

Table 1. *Cont.*

Items	Description
Basic observables	Double-differenced, ionosphere-free combination of L1 and L2 carrier phases. Pseudoranges are used only to obtain receiver clock offsets and in ambiguity resolution when performing Melbourne–Wuebbena wide-lane method. Nonredundant double differences are used. Elevation angle cutoff: (a) 3 degrees (b) 10 degrees, Sampling rate: 30 s for cleaning; 2 min in least squares analysis
Modeled observables	Double-differenced carrier phase with ionosphere-free linear combination applied. Clocks are estimated in a post-processing step using one-way observables, with the ensemble mean of the clock residuals at a set of reference ground stations set to zero at each epoch.
Troposphere	Zenith delay: Saastamoinen (1972) [34] "dry" + "wet" Mapping function: GPT3 with $1° \times 1°$ global grid
Ionosphere	1st order effect: accounted for by dual-frequency observations in linear combination.
Tidal	Solid Earth tide, pole tide, ocean tide loading corrections according to IERS Conventions 2010.
Orbit models	Final precise orbits and clock products from IGS.
Phase center offset (satellite)	Corrected using IGS values for all GPS satellites.
Receiver antenna PCOs and PCVs	PCO and PCV corrections for GPS are from igs14_2233.atx.
Terrestrial frame	IGb14
Orbits	IGS final orbits

3. Results

3.1. Carrier Phase RMS and A-RMS

From a total of 55 GNSS stations, only 23 stations had more than 95% of the data available for the entire year to be processed. In the case of these stations, for the RMS and A-RMS of the LC, three types of statistics were computed: the minimum value (Min), the average value (Avg) and the maximum value (Max). The results are presented in Table 2.

A small value of the LC RMS scatter showed lower levels of noise, whereas the high level of noise was indicated by a high value of RMS. A max value, although it looked wrong, did not necessarily represent a bad value. The high level of noise can be generated by turbulence in the atmosphere or a local environment which may create a noise phase scatter. Using the two different processing strategies for all of the stations, except station TRF2 and OPMT, we found that the 10° strategy showed a lower level of noise, due to the elimination of much nosier data.

The stations with the highest average LC phase residuals in the case of the 3° elevation angle were REYK, TLMF and CAKO with 17.2 mm, 16.8 mm and 16.6 mm, whereas in the case of the 10° elevation angle, they were REYK, CNIV and SCOA with 11.6 mm, 10.8 mm and 10.2 mm. In both cases, the REYK showed the highest value. If we differentiate the averaged LC phase residuals between the two processing strategies, then GNSS stations CAKO, ILDX and TLMF had the highest differences of −8.4, −8.4 and −8.1. Therefore, basically the RMS phase scatter in the case of station CAKO degraded by 50% when using a 3° elevation angle processing strategy. When using the A-RMS as a statistic to evaluate the results, it can be observed that the highest values in the case of the 3° elevation angle were present at stations CNIV, REYK and CAKO with 12.5 mm, 12.4 mm and 12.3 mm, while in the case of the 10° elevation angle, stations REYK, CNIV and SCOA showed the highest A-RMS with 8.5 mm, 8.3 mm and 6.7 mm. If we differentiate the averaged A-RMS phase residuals between the two processing strategies, GNSS stations TLMF, ILDX and CAKO had the highest differences of −6.5, −6.5 and −6.3. A metric for the type of scatter, by using the ratio between the 25-point average RMS and the single-point RMS, showed in both cases the presence of short-term noise, except CNIV, CAKO, ILDX and REYK, which showed the presence of stronger-than-usual dominance of long period variation.

Table 2. The stations that had more than 95% of the data available to be processed and with the following statistics: min, average and max for the RMS and A-RMS.

	Cutoff Elevation Angle																	
	3°			10°						3°			10°					
	RMS			RMS			Diff. 10°–3°			A-RMS			A-RMS			Diff. 10°–3°		
Sta.	Min	Avg	Max	Min	Avg	Max	Min	Avg	Max	Min	Avg	Max	Min	Avg	Max	Min	Avg	Max
BOLG	5.8	9.5	24.8	5.2	7.1	18.1	−0.6	−2.3	−6.7	2.6	6.3	20.1	2.1	4.5	15.2	−0.5	−1.8	−4.9
CAKO	10.5	16.6	40.0	6.5	8.3	15.5	−4.0	−8.4	−24.5	7.5	12.3	29.9	4.2	6.0	13.0	−3.3	−6.3	−16.9
CNIV	11.5	16.5	29.1	9.7	10.8	18.3	−1.8	−5.7	−10.8	8.4	12.5	24.3	7.1	8.3	15.5	−1.3	−4.2	−8.8
DEVA	6.8	10.1	19.5	5.3	7.7	15.4	−1.5	−2.4	−4.1	3.9	6.8	16.1	2.6	4.8	12.3	−1.3	−2.0	−3.8
GLSV	7.9	15.2	32.1	6.3	7.8	16.2	−1.6	−7.4	−15.9	4.6	10.7	25.1	3.2	4.8	13.0	−1.4	−5.9	−12.1
HOFN	8.8	13.5	23.6	6.2	7.9	12.3	−2.6	−5.6	−11.3	4.6	8.9	18.2	2.8	4.6	9.5	−1.8	−4.2	−8.7
IGEO	8.1	13.4	27.0	5.8	7.4	14.4	−2.3	−6.0	−12.6	4.7	9.6	22.5	2.8	4.6	11.9	−1.9	−4.9	−10.6
ILDX	9.5	16.4	40.2	5.5	8.0	14.2	−4.0	−8.4	−26.0	6.7	12.2	33.6	3.8	5.7	11.7	−2.9	−6.5	−21.9
KIR0	7.6	11.3	20.6	4.4	6.5	10.8	−3.2	−4.9	−9.8	3.9	7.5	15.6	2.4	4.2	8.6	−1.5	−3.4	−7.0
KLOP	8.3	10.3	15.9	8.5	10.1	14.6	0.2	−0.2	−1.3	3.4	5.2	11.3	3.2	4.9	10.4	−0.2	−0.3	−0.9
MDVJ	7.9	12.0	26.7	6.2	8.2	14.6	−1.7	−3.8	−12.1	4.4	8.0	20.2	3.1	5.1	11.2	−1.3	−2.9	−9.0
MOPI	7.5	10.7	17.7	7.1	9.5	13.1	−0.4	−1.2	−4.6	4.2	6.7	13.6	4.0	5.6	9.6	−0.2	−1.1	−4.0
OPMT	7.0	8.3	12.2	7.0	8.3	12.1	0.0	0.0	−0.1	3.9	5.2	9.4	3.8	5.2	9.1	−0.1	−0.1	−0.3
PTBB	7.2	11.0	20.4	5.4	7.4	13.9	−1.8	−3.5	−6.5	4.0	7.4	16.0	2.7	4.8	11.1	−1.3	−2.6	−4.9
REYK	12.4	17.2	28.2	9.4	11.6	16.3	−3.0	−5.6	−11.9	7.9	12.4	22.2	6.4	8.5	13.6	−1.5	−3.9	−8.6
RIGA	8.1	10.8	18.2	6.5	8.2	13.1	−1.6	−2.6	−5.1	3.5	6.6	14.0	2.6	4.4	9.7	−0.9	−2.2	−4.3
SCOA	10.9	15.3	25.1	7.4	10.2	15.5	−3.5	−5.2	−9.6	6.5	10.9	20.3	4.5	6.7	11.9	−2.0	−4.2	−8.4
SFER	5.5	13.3	28.5	4.0	6.1	13.5	−1.5	−7.2	−15.0	3.0	9.9	24.2	2.1	4.2	10.8	−0.9	−5.7	−13.4
SMLA	7.6	13.4	30.5	5.6	7.3	15.7	−2.0	−6.1	−14.8	4.2	9.3	24.6	2.8	4.6	12.2	−1.4	−4.7	−12.4
TLMF	10.7	16.8	29.5	7.3	8.7	15.8	−3.4	−8.1	−13.7	6.0	11.6	24.9	3.3	5.1	11.7	−2.7	−6.5	−13.2
TRF2	6.7	8.4	14.6	7.7	8.9	14.9	1.0	0.5	0.3	2.6	4.3	11.0	2.9	4.5	11.5	0.3	0.2	0.5
WAB2	7.5	14.6	33.0	5.1	6.7	17.0	−2.4	−7.9	−16.0	4.0	9.4	25.8	2.4	4.3	13.8	−1.6	−5.1	−12.0
YEBE	8.2	12.2	23.2	7.1	8.8	14.9	−1.1	−3.5	−8.3	4.5	7.9	17.8	2.8	5.1	12.5	−1.7	−2.7	−5.3

In order to observe the behavior of the LC phase RMS and A-RMS under the two elevation angles, 3° and 10°, and whether the scatter is correlated to the quantity of precipitable water vapor (PWV) in the troposphere, the processed data are presented in Figure 1. The PWV was extracted from the wet zenith total delay which was estimated from the GPS observation. First, the zenith total delay estimates were extracted, then the corrections for the hydrostatic delay were applied and afterwards they converted the residual wet delay to precipitable water. The tropospheric delay effect was used to model a priori the delay—the so-called zenith total delay (ZTD)—and relate the ZTD to the delay according to any elevation angle throughout using a specified mapping function (in our case, GPT3) and to estimate discrete corrections to the a priori ZTD model to capture the time-varying nature of the troposphere [35]. The corrections to the ZTD were estimated using partial derivatives that related wet delays to the phase observations [35].

The a priori pressure and temperature for a site came from the global pressure and temperature model GPT3. The PWV was computed with a resolution of 30 min and then we averaged it for the entire day. The station CAKO was used as an example.
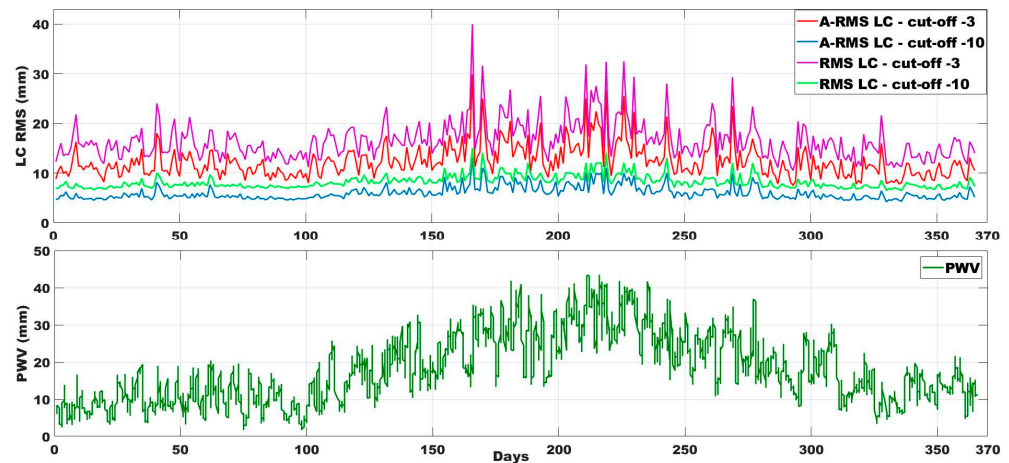
Figure 1. Station CAKO: RMS and A-RMS values are in the upper part and PWV in the lower part.

Each day was analyzed individually between the LC phase and PWV in batches of four hours for analyzing the correlation between the two estimates. From the Figure 1, we can observe that the dominant source of error for the phase scatter was the presence of water vapor in the troposphere, which showed a correlation time of a few days. The correlation coefficient between PWV and RMS for the 3° was 0.66 and for the 10° was 0.76, thus the results showed a stronger correlation for the data that were processed at the 10° elevation cutoff. The occurrence of extreme values in the daily variability was associated with the increased presence of the PWV. Neglecting the aforementioned correlation will lead to uncertainties that are too optimistic. The comparison in terms of LC phase RMS between the 3° cutoff elevation angle and 10° cutoff elevation angle showed that, in the second strategy, the LC RMS had a mean value of 8.3 mm, compared to the first strategy, where we obtained 16.6 mm, twice the value when compared to the first strategy. This is due to the fact that on day 166, the LC phase residual experienced an extreme value of 40 mm using the first strategy, which was an increase of almost 2.5 times compared to the mean value. In the second case, the extreme value was 15.5 mm, which represented an increase of ~1.9 times, so the maximum deviation from the mean was slightly reduced. Moreover, the deviation from the mean value in the first case for the period (day of year, DOY) 166~262, which represented the period with the highest LC RMS, was around 1.4 times, whereas in the case of the second strategy it was ~1.25 times. If we analyzed the entire period, in the case of the 3° cutoff elevation angle, the deviation from the mean was higher than in the second case (10° elevation angle cutoff). Another important conclusion was that in both cases, the pattern of the RMS scatter was relatively similar.

In the case of the A-RMS, the daily variability was much more constant during the year in both cases, and the mean values were reduced for the 3° elevation angle by ~26% and for the 10° elevation angle by ~28%. The A-RMS tended to have a higher influence on the mean values than on the maximum values, while the improvement of the phase scatter in the case of the 3° elevation angle was 25%, whereas in the case of the 10° elevation angle it was only 16%. For the minimum values in the first case, the improvement was 27%, and in the second case, it was 35%. The effect of PWV on the LC phase scatter can be seen (as expected) especially on the 3° elevation angle processing strategy. The correlation coefficient between PWV and A-RMS for the 3° was 0.68 and for the 10° was 0.76, and thus the results show a stronger correlation for the data that were processed at the 10° elevation cutoff. This can be the effect of a greater concentration of PWV at higher elevation.

The correlation for all the stations between the RMS, A-RMS and PWV for the two elevation angles, 3° and 10°, is presented in Figure 2. The Figure 2b, with the spatial distribution for the correlation coefficient, presents explicitly the highest and lowest correlation coefficient and also the exemplified station CAKO. It can be observed that 20 out of 55 stations showed a strong correlation with a correlation coefficient higher than 0.6;

32 out of 55 stations showed a moderate correlation with a correlation coefficient between 0.4 and 0.59; and only 3 out of 55 stations showed a weak correlation with a correlation coefficient lower than 0.4. The classification of the correlation magnitude was declared according to [36].
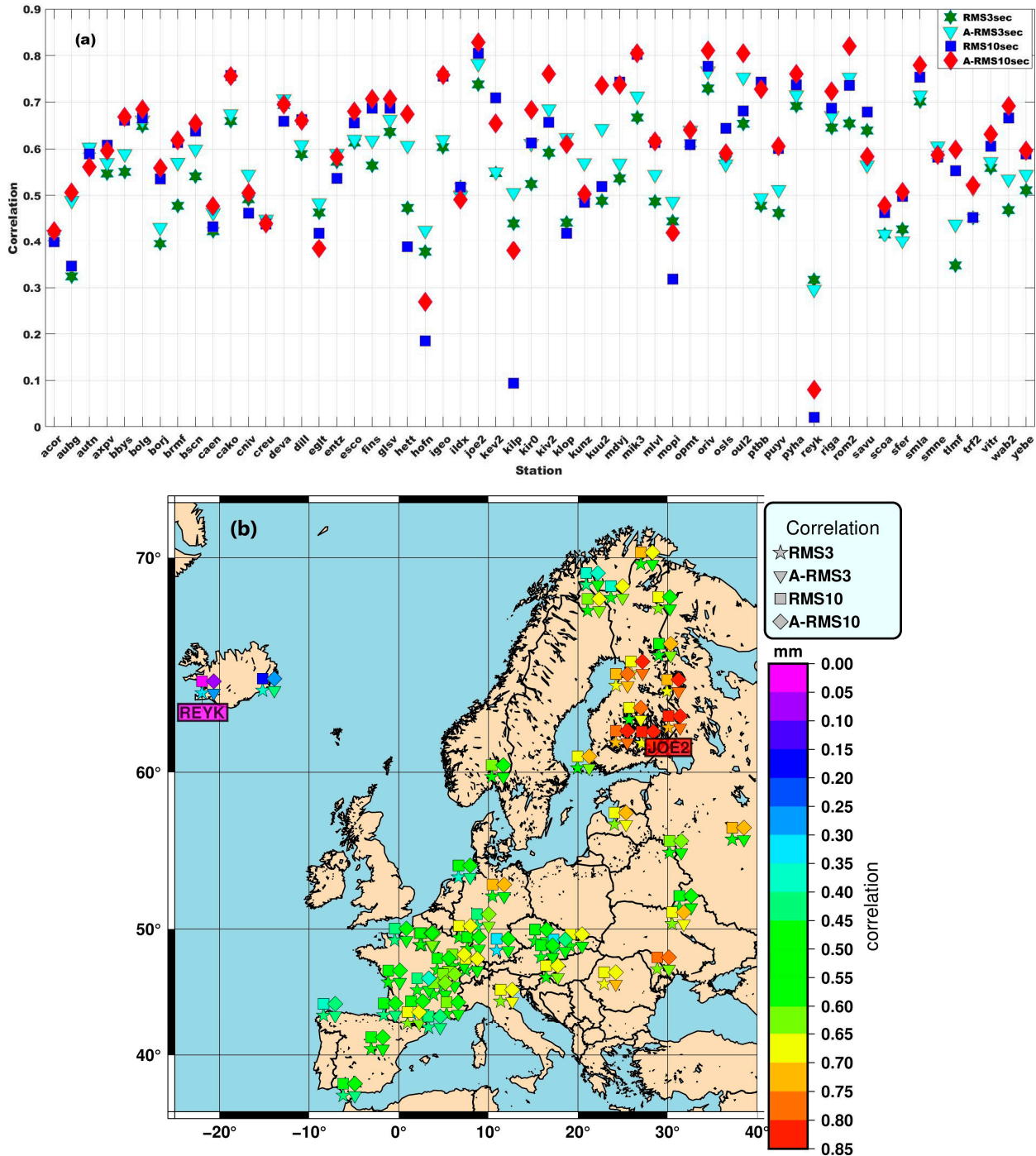

Figure 2. The correlation coefficient between the RMS, A-RMS and PWV for the two elevation angles, 3° and 10°. Top panel: (**a**) the distribution of the values, and bottom panel: (**b**) spatial distribution of the correlation coefficient.

The GNSS stations situated in Finland showed a higher correlation for all four processing strategies.

The specific day of the year of a GNSS station when the maximum value of the averaged LC phase RMS scatter occurred is presented in Figure 3, which illustrates the temporal and spatial distribution of the averaged LC phase RMS for the 10° and 3° cutoff elevation angles. The highlighted stations represent the following: CAKO—the station that is used as an example in Figure 1; BORJ—the station that showed the highest LC phase residual when using the 3° cutoff elevation strategy; and station REYK—the station that presented the highest LC phase residual when using the 10° cutoff elevation angle processing strategy.
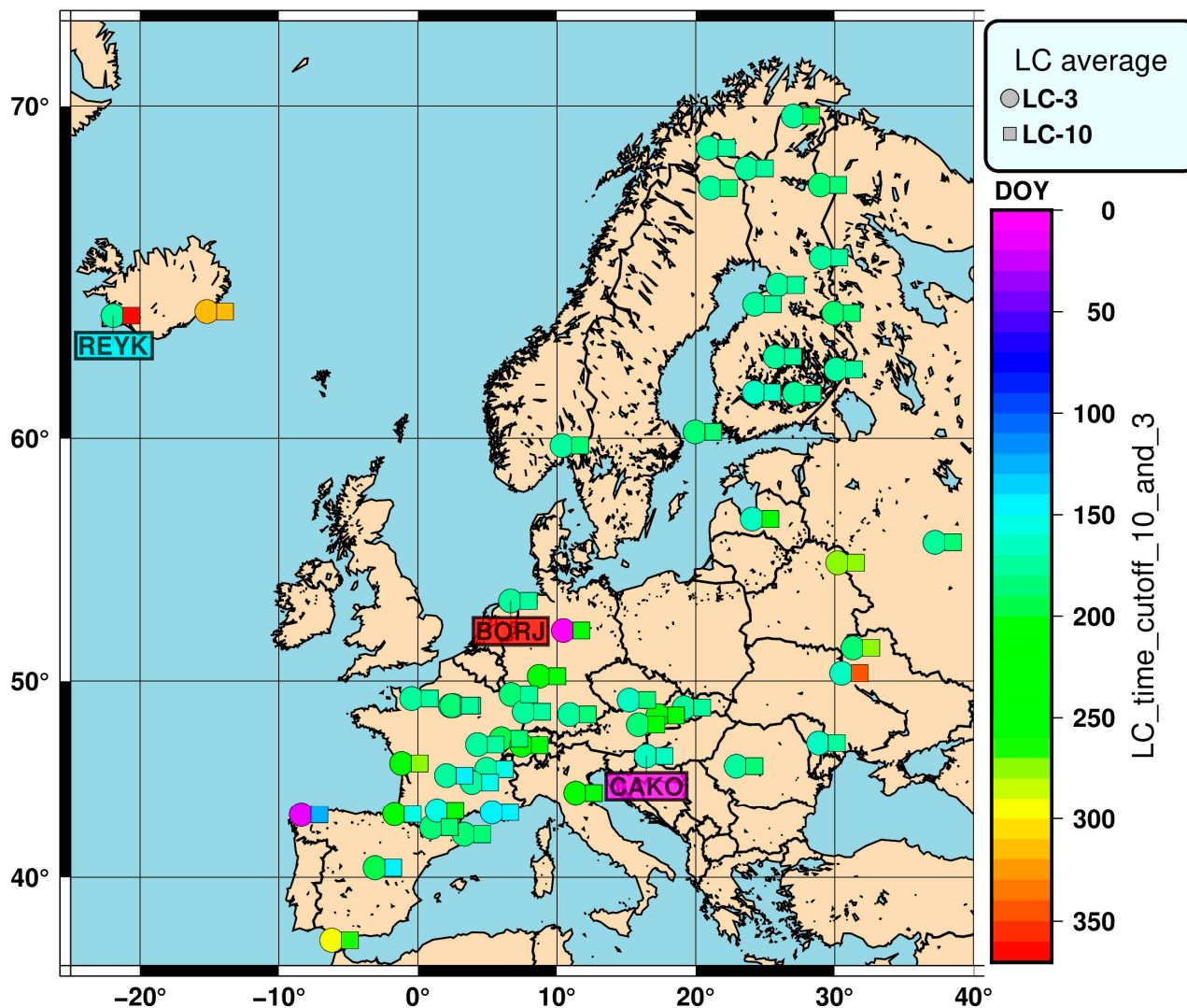
Figure 3. Temporal and spatial distribution of the averaged LC phase RMS for the 10° and 3° cutoff elevation angle.

The averaged LC phase RMS values for the 3° cutoff elevation angle and 10° cutoff elevation angle are presented in Figure 4. In conjunction with the results presented in Figure 3, in the results from Figure 4 with the averaged LC phase scatter, we can see that the results in both strategies showed the lowest values of the LC RMS at the stations located in the northern part of Europe. The RMS values increased as we moved to the central part of Europe. Thus, around 85% of the stations presented the highest averaged value during the day of year (DOY) between 150 and 240 which represented the summer period, whereas in the period 245–280 DOY, we had around 8%, and the other 7% showed the maximum averaged values in the intervals 8–9 DOY and 310–362 DOY.
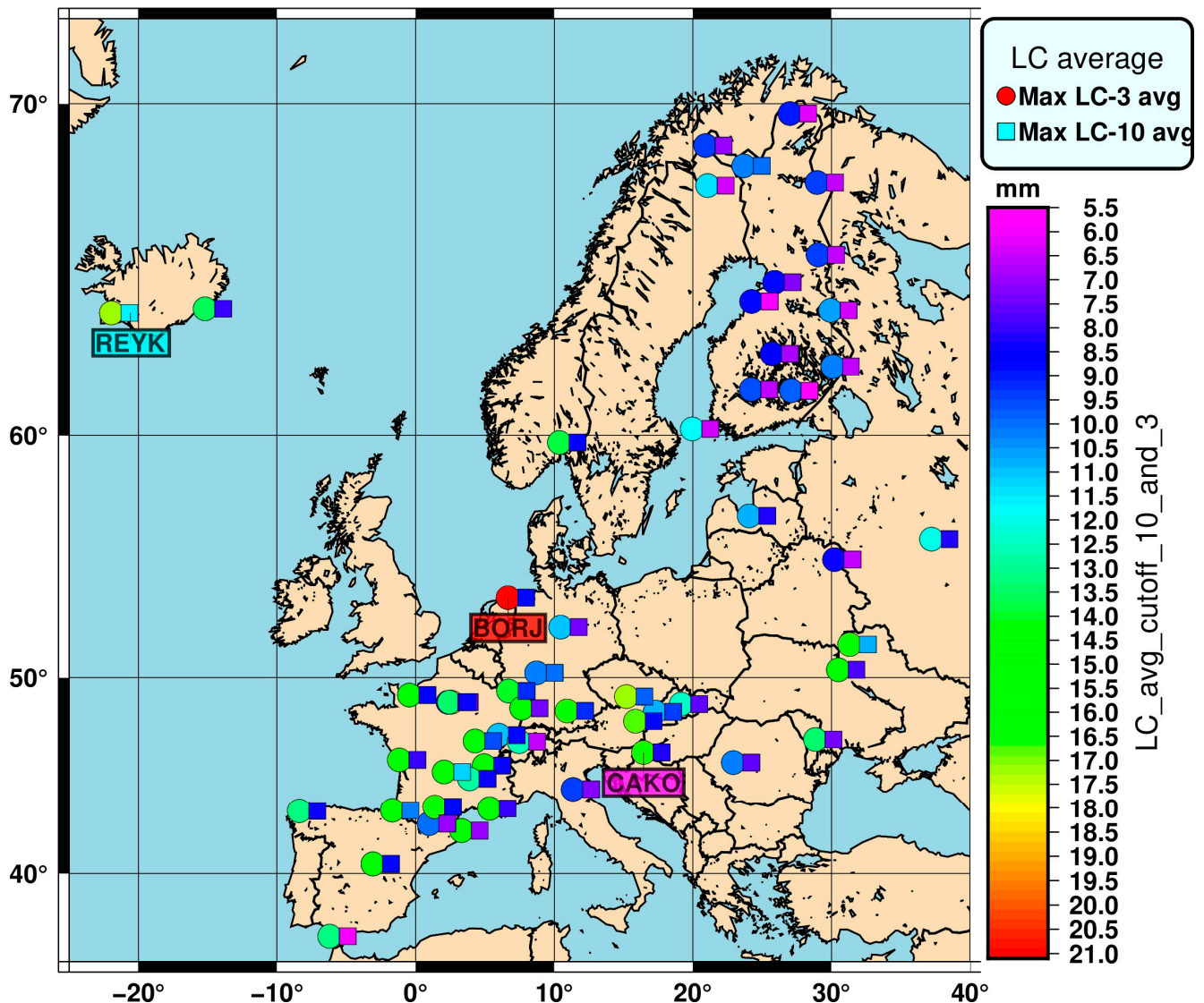
Figure 4. The averaged LC phase RMS values for the 3° cutoff elevation and 10° cutoff elevation angles.

The results presented in Figure 4 show that approximately 90% of the stations showed a lower LC phase RMS when using a 10° cutoff elevation angle compared to the results when using a 3° cutoff elevation angle strategy. This can be explained by the fact that the multipath effect has the tendency to increase when using a lower satellite elevation angle because the instantaneous effect of the multipath is generally merged with phase noise but also because the signal becomes noisier due to the longer distance that it has to travel to the troposphere for the low elevation satellites. The phase analysis is not the final goal itself; the goal is to have a positioning benefit, which will be analyzed further.

3.2. The Station Coordinates' Repeatability for the North (N), East (E) and Up Component under 3° and 10° Cutoff Elevation Angle

Due to the nature of the comparison between the results for the two different cutoff elevation angles, we compared the WRMS results of the station coordinate representing their repeatability on all three components: North, East and Up. First, the histogram of A-RMS for each component is presented in Figure 5.
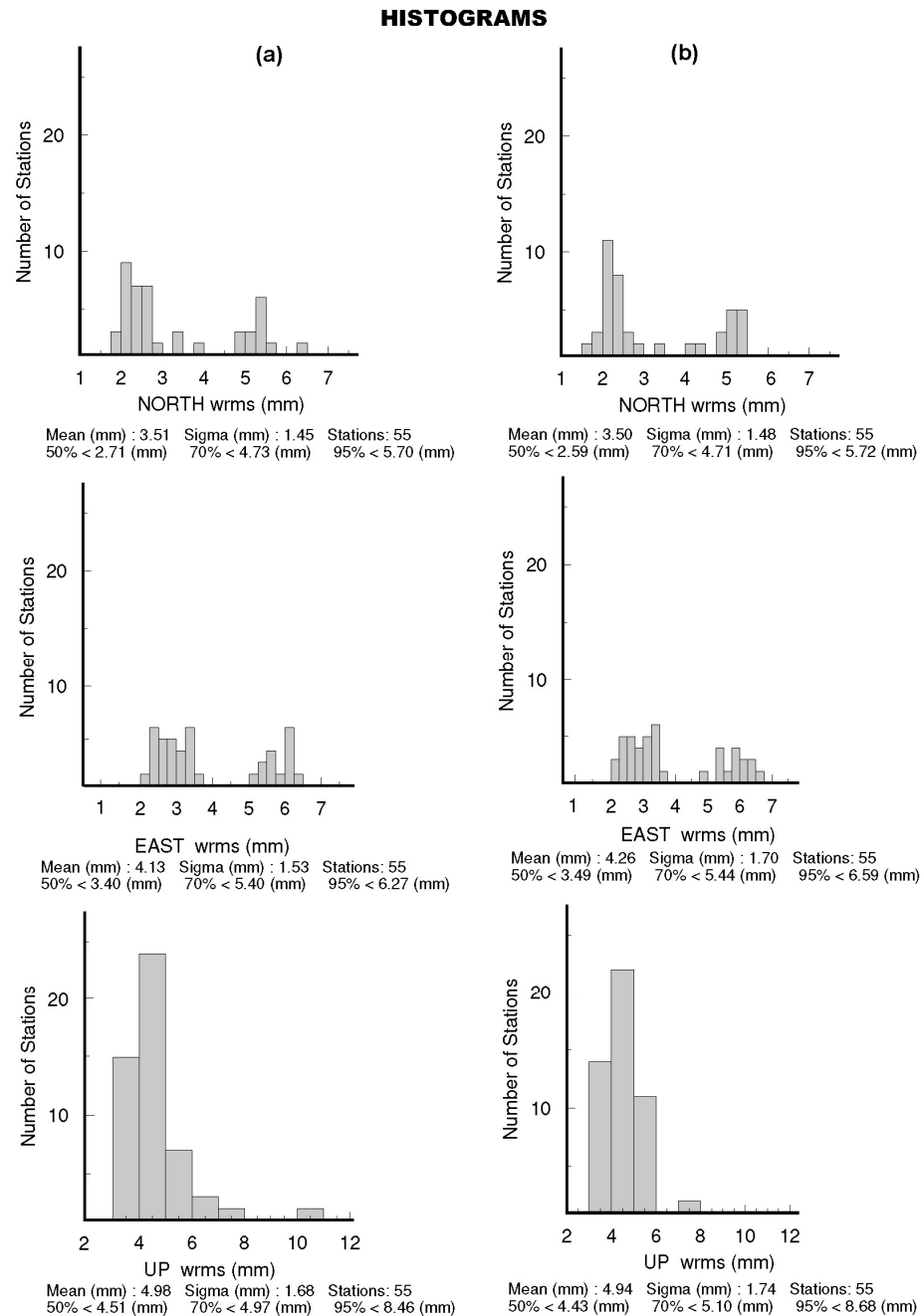
HISTOGRAMS

Figure 5. Statistical histogram of A-RMS of the WRMS scatter between the position estimates for the (**a**) 3° cutoff elevation angle and (**b**) 10° cutoff elevation angle.

The analyses were conducted on all 55 stations, not only on those which had more than 95% of the available data for 2020. The difference in the mean WRMS scatter for the North component between the two-computing strategy was 0.01 mm, but for the median WRMS scatter the difference was 0.12 mm, with a higher median value for the 3° elevation angle. For the rest of the percentage comparison for the 70% and 95%, the difference was similar as for the mean difference. For the East component, the difference in mean values of the WRMS scatter was higher, 0.13 mm, but the median WRMS scatter was 0.09 mm. The highest difference can be observed at 95% of the data, with a value of 0.32 mm. In the case of the Up component, the difference in the WRMS scatter of the (a) mean was 0.04 mm, (b) median was 0.08 mm and for the rest of the statistics was growing from 0.13 mm to 0.22 mm in the case of 95% of the data. The variability for the Up component for station CAKO is presented in Figure 6, as a representative example.
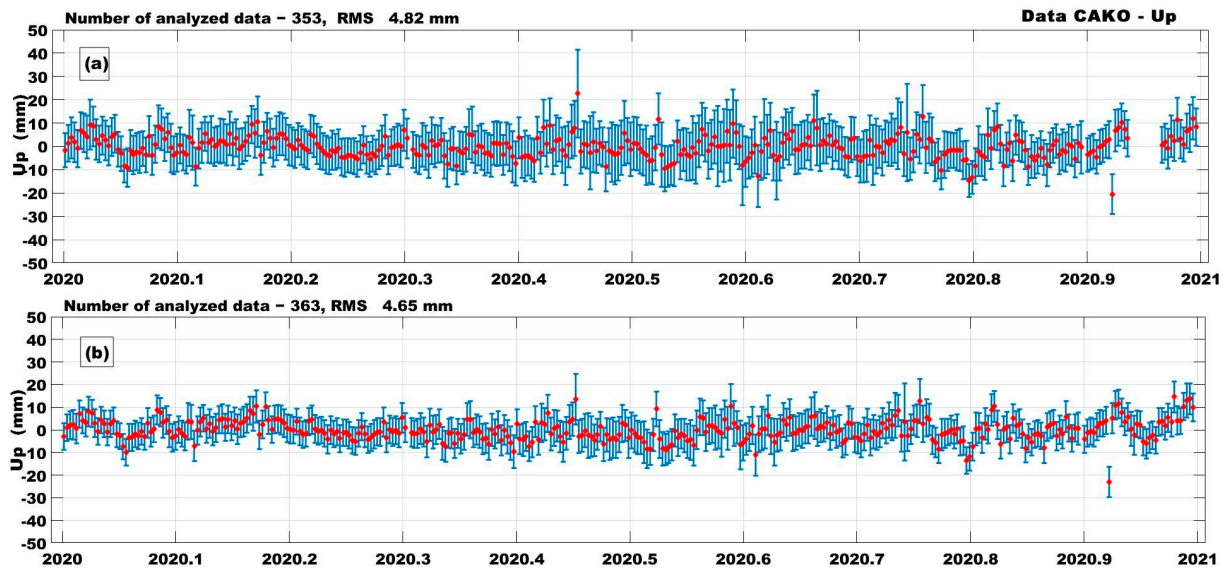
Figure 6. Daily variability for the Up component of station CAKO: Top panel: (**a**) using a 3° cutoff elevation angle; and bottom panel: (**b**) using a 10° cutoff elevation angle.

The daily position is represented by the red dots, and the blue line represents the error bar for each individual value. Based on the analysis, it can be noticed that in the case of the 3° cutoff elevation angle, at the end of 2020, around 10 days' worth of data were removed after using the χ^2 test for the detection and removal of outliers from the final combined solution. The RMS in the case of the 3° cutoff elevation angle (case (a)) was higher when compared to using a 10° cutoff elevation angle (case (b)), with a value of 4.82 mm and 4.65 mm, respectively. We can notice that in case (a) the error bars were almost 1.5 times higher than in case (b). In case (a), there was a variability of daily positions that reached a value of 23 mm on the 14th of June, whereas in case (b), the daily variability was around 14 mm. The other extreme value was on the 3rd of December, but this time in case (a) we had a large value of 23 mm, whereas in case (b) the daily variability reached 21 mm. Thus, the daily variability in the case where we eliminated the extreme value (those higher than 7 mm), the difference between the two cases did not reach 2~3 mm.

Figure 7 presents the WRMS scatter of the difference between the 10° cutoff elevation angle and the 3° cutoff elevation angle for the North component, after detrending, i.e., removing the linear trends, offsets and the annual and semi-annual sine and cosine terms using the maximum likelihood estimation [37].

One can see that the largest difference in the WRMS scatter for the North component was for station YEBE, which is located in the central part of Spain, with a value of −0.16 mm. We can observe that the largest differences between the two different cutoff elevation angles were in the western and central part of Europe, and that those were negative differences (this means that for a cutoff elevation angle of 3°, we had a higher WRMS when compared to a 10° cutoff elevation angle). Furthermore, the majority of the GNSS stations located in the mainland of the continent experienced higher differences than the stations located in the coastal area. The GNSS stations located in Iceland and in the upper part of Scandinavia plus Belarus (station VITR) had mainly positive differences between the two strategies.

Likewise, Figure 8 shows the WRMS scatter of the difference between the 10° cutoff elevation angle and the 3° cutoff elevation angle for the East component, after detrending by removing the linear trends, offsets and the annual and semi-annual sine and cosine terms.
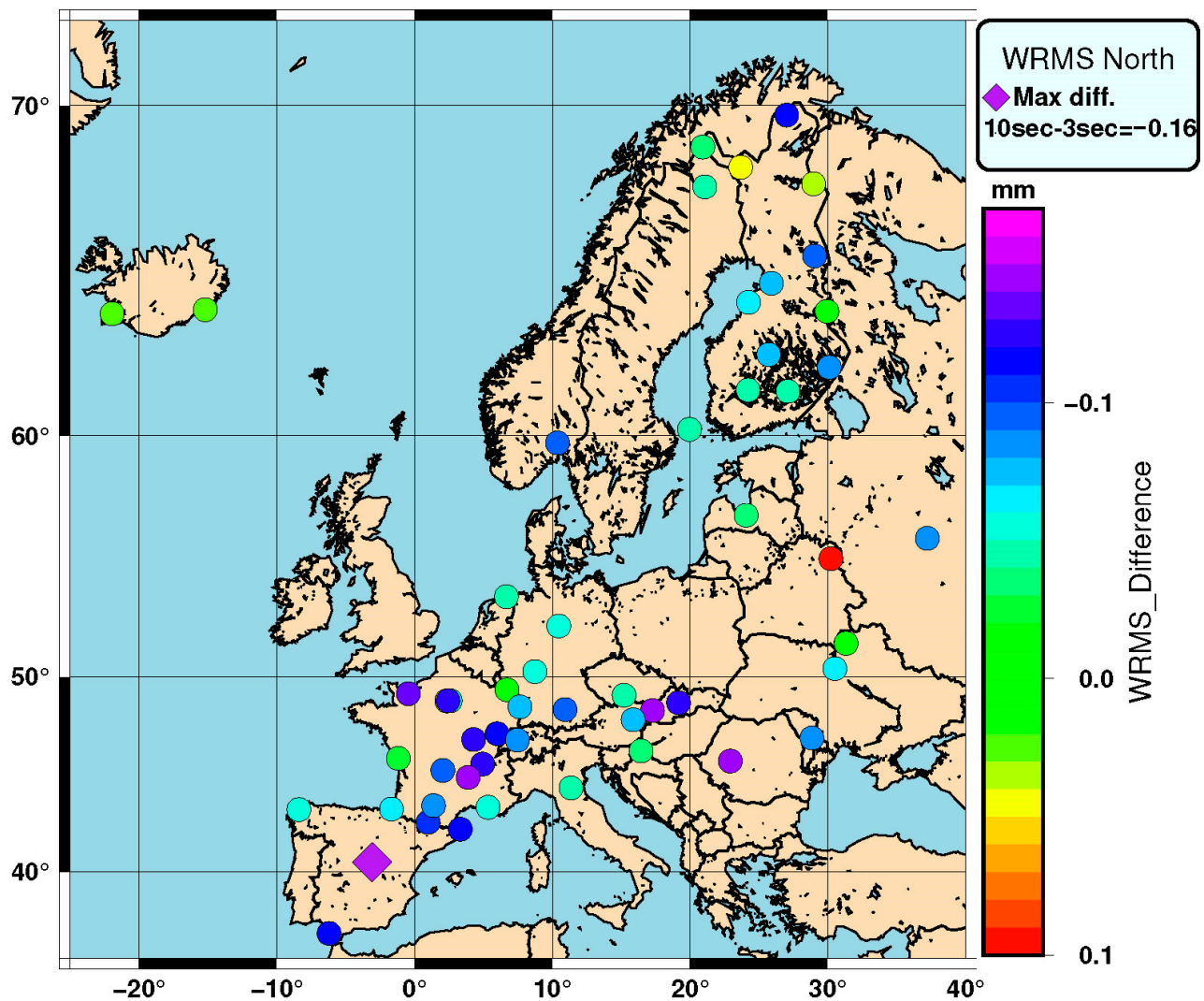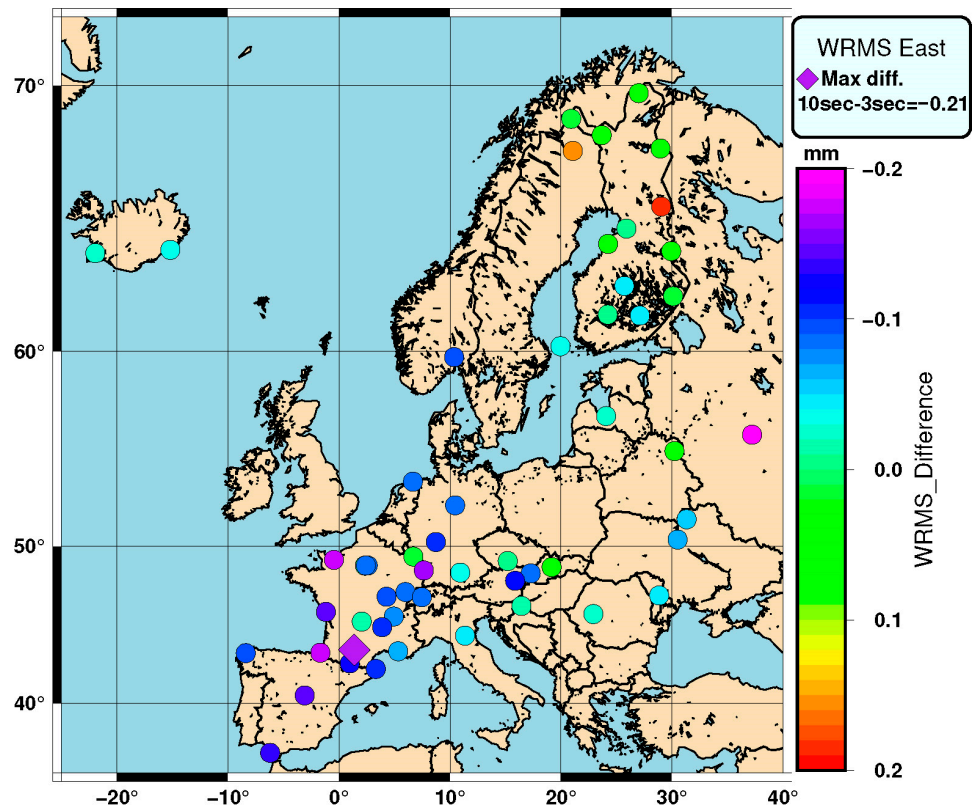
Figure 7. WRMS scatter of the difference between 10° and 3° cutoff elevation for the North component, after removing the linear trends, offsets, annual and semi-annual sine and cosine terms.

Figure 8 depicts that the largest difference in the WRMS scatter for the East component was for station TLMF, located in the southwest part of France, with a value of −0.21 mm. We can observe that there are another three stations located in France (CAEN, SCOA and ENTZ) that had a large WRMS scatter difference of ~0.20 mm. In the western and central part of Europe, we had the largest differences between the two different cutoff elevation angle approaches, and these differences were negative, just as in the case of the North component. There were no visible differences between the GNSS stations located in the continent mainland when compared to the stations located in the coastal area. The GNSS stations located in the upper part of Scandinavia, plus Belarus (station VITR), had mainly positive differences between the two strategies, with a maximum of 0.18 mm for station KUU2.

In general, the pattern of the WRMS scatter for the results when using the 10° cutoff elevation angle and the 3° cutoff elevation angle strategies for the North and East component was very similar, as illustrated in Figure 9.
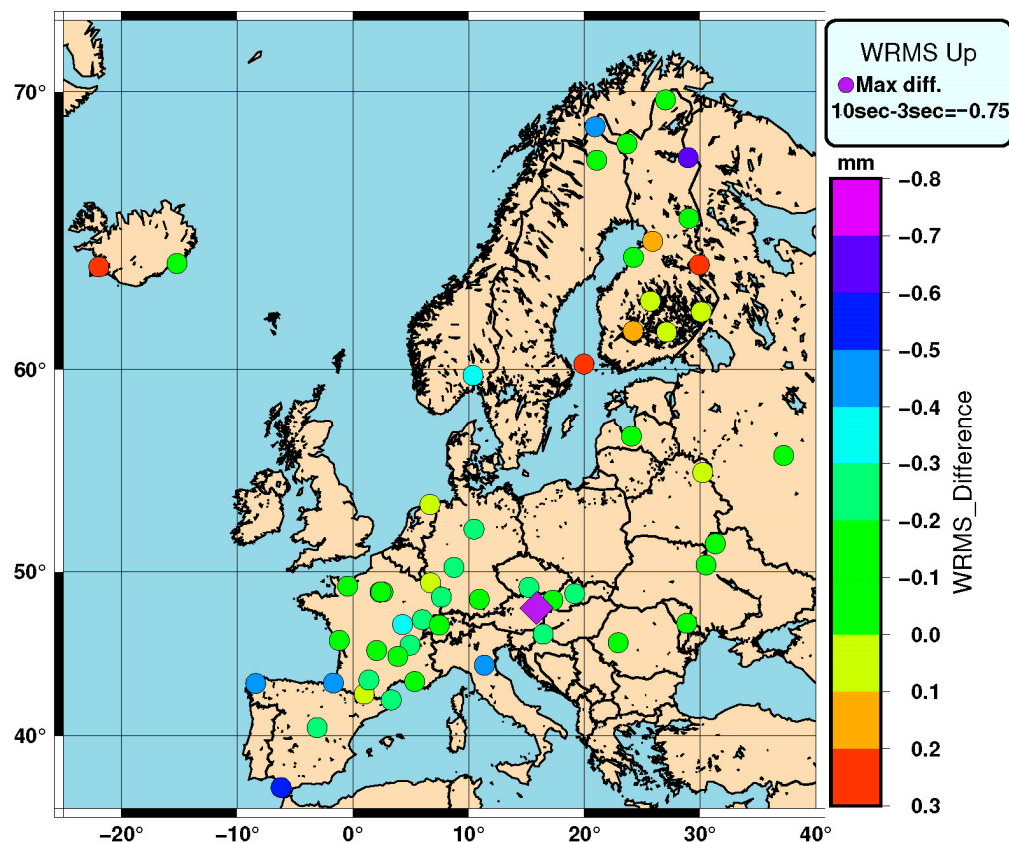
Figure 8. WRMS scatter of the difference between $10°$ and $3°$ cutoff elevation for the East component, after removing the linear trends, offsets, annual and semi-annual sine and cosine terms.
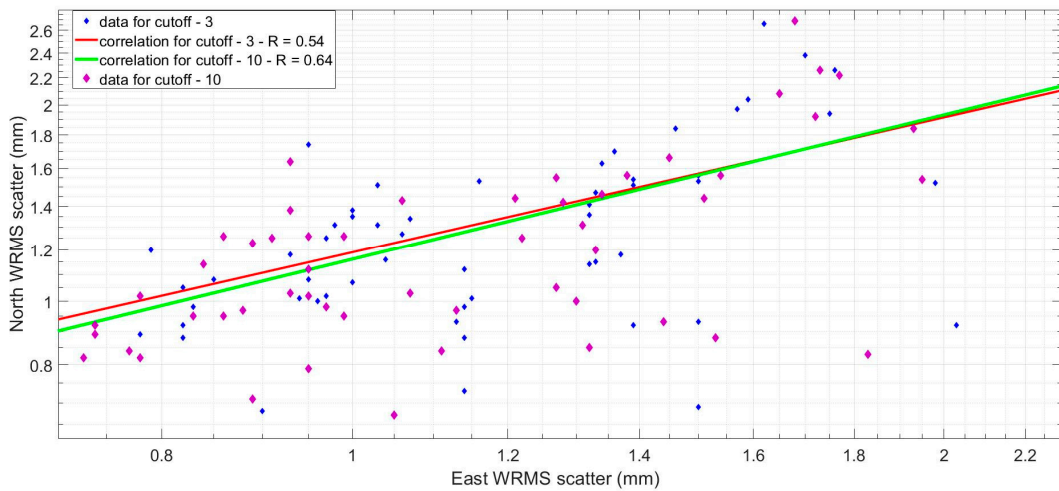
Figure 9. Log–log plot for the North and East WRMS scatter of the 55 GNSS stations. The solid green line shows the correlation for the results by using a $10°$ cutoff elevation angle and the red line presents the results for the $3°$ cutoff elevation angle.

It can be seen from the plot that the WRMS scatter of the North component in both cases—using the $10°$ cutoff elevation angle and the $3°$ cutoff elevation angle—had a larger WRMS value compared to the East component. When comparing between the two strategies, the correlation coefficient for the $10°$ cutoff elevation angle showed a higher correlation between the North WRMS and East WRMS with a correlation of 0.64, whereas for the $3°$ cutoff elevation angle, the correlation coefficient was 0.54. Thus, the strength of the correlation in the case of the $10°$ cutoff elevation angle was considered to be strong, whereas in the case of the $3°$ cutoff elevation angle, the correlation strength was moderate.

The WRMS scatter of the Up component for the difference between the 10° cutoff elevation angle and 3° cutoff elevation angle after detrending by removing the linear trends, offsets, annual and semi-annual sine and cosine terms is shown in Figure 10.

Figure 10. WRMS scatter of the difference between 10° and 3° cutoff elevation for the Up component, after removing the linear trends, offsets, annual and semi-annual sine and cosine terms.

From Figure 10, the highest difference in the WRMS scatter for the vertical position estimates was found at station TRF2, a GNSS station located in the eastern part of Austria, with a value of −0.75 mm. The next GNSS stations that had a high difference in the WRMS scatter were in Finland (two stations), and one further station in Spain. There were no clear signs that the GNSS stations located in the mainland experienced higher differences compared to the stations located in the coastal area, except for the Iberian Peninsula. Regarding the differences in the WRMS scatter of the vertical position estimates, the GNSS stations located in the upper part of Scandinavia, Belarus (station VITR) and Iceland had mainly positive differences between the two strategies (just as in the case of the horizontal component), with a maximum of 0.27 mm for stations ROM2 and REYK.

The correlation between the GNSS station latitude and WRMS is illustrated in Figure 11 for the three position coordinates North, East and Up, from the top to bottom panels, respectively.

It can be seen from Figure 11 that the correlation coefficient was higher for all three components for the strategy of computing the data at a 10° cutoff elevation angle compared to a 3° cutoff elevation. The correlation coefficient for the East and North components presented a strong correlation between the WRMS and latitude of the stations, whereas for the Up component, the correlation was moderate.
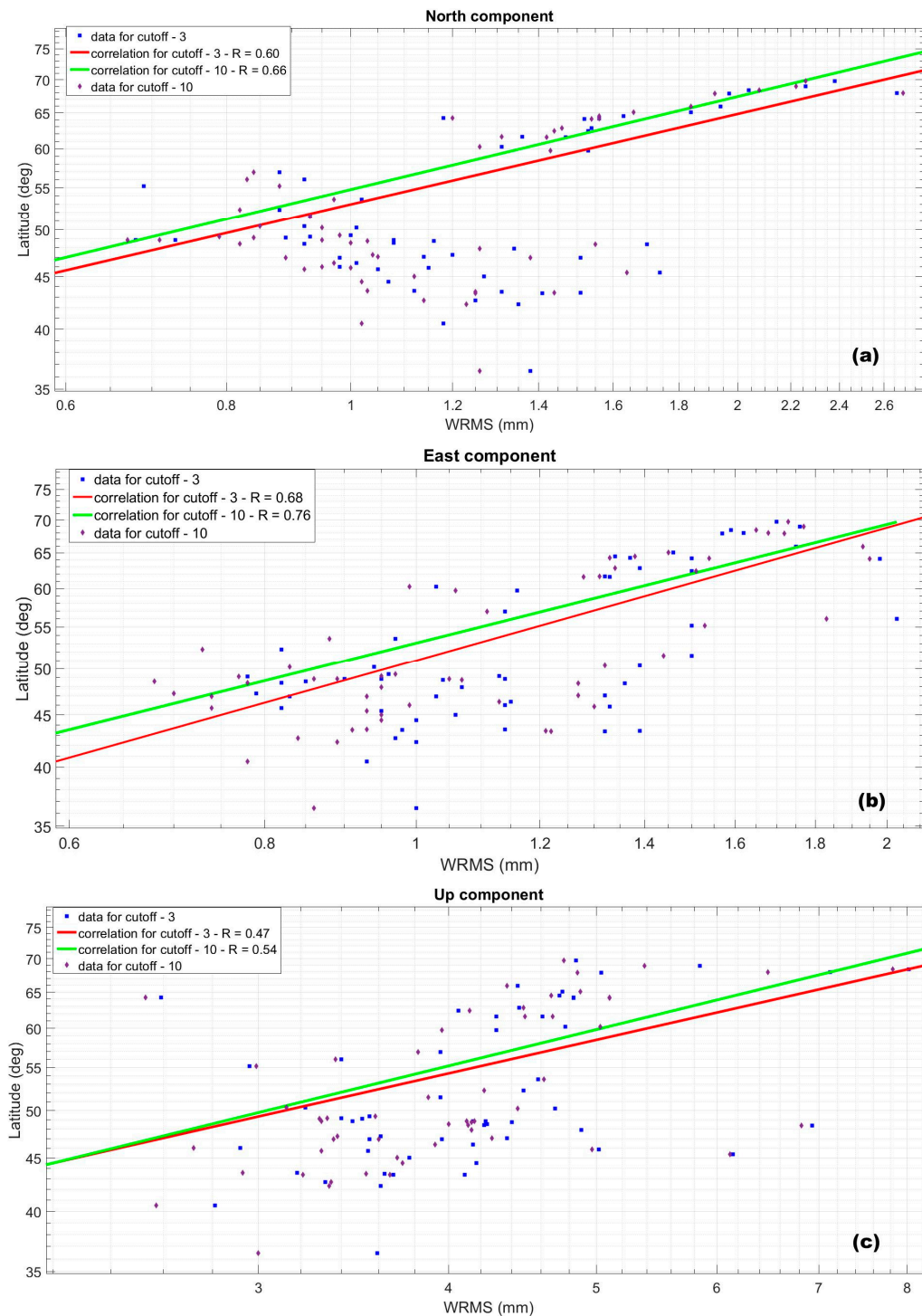
Figure 11. The correlation between the GNSS station latitude and WRMS for (**a**) North component, (**b**) East component and (**c**) Up component.

4. Discussion and Conclusions

One objective of this study is to demonstrate for GNSS users the impact of selecting the elevation cutoff angles, as the majority of users follow typical values without quantifying this impact. Moreover, to assess the data quality and different environmental characteristics for each individual GNSS station, a detailed analysis of the phase observations is recommended. According to [24], the common values of the RMS scatter that we should obtain for the ionosphere-free linear combination residuals are ~6–9 mm, but due to a difference in conditions around the GNSS antennas that can generate multipath scattering, the residuals

will vary in azimuth and elevation around the horizon. There are also cases where large phase residuals can indicate incorrect antenna models. The difference of the LC phase RMS scatter presented in Table 1, between the 10° cutoff elevation angle and 3° cutoff elevation angle, can indicate not only the effects of the local environment or atmospheric fluctuations, but also how much the possible outliers from the LC phase RMS can affect the averaged value and which strategy shows cleaner LC phase data. For the LC RMS in case (a), the result by using the 3° cutoff elevation angle processing strategy is ~8–18 mm, whereas in case (b), the result by using the 10° cutoff elevation angle processing strategy for the LC RMS scatter is ~6–12 mm. Approximately 90% of the stations show a lower LC phase RMS between 30% and 50% when using a 10° cutoff elevation angle compared to the results when using a 3° cutoff elevation angle strategy, whereas the only two GNSS stations—namely, OPMT and TRF2—show a better LC phase RMS in the case of using a 3° cutoff elevation processing strategy.

In Figure 1, it can be noticed that during summer, the phase RMS and the A-RMS scatter are larger until the end of September, then they start to drop down. The quantity of the water vapor has large fluctuations in summer and autumn and less in winter and spring, thus the increase in the RMS scatter during summer and autumn is related to the water vapor, which reaches much higher absolute values and spatiotemporal variability.

Although the mean value of the LC phase RMS is not high, the temporal behavior is quite complex in both cases, and it shows a strong correlation between the increase in PWV and the LC phase RMS in the case of the station CAKO. There is a strong dependence between the PWV and the cutoff elevation angle, which can be seen in Figure 1, whereas the accuracy of the GNSS-derived PWV is affected by elevation angle-dependent errors, which are more noticeable at a lower elevation cutoff angle which is supported by the findings of [38,39]. Also, it can be observed in Figure 1, and in interconnection with Figure 6, that the presence of the seasonal signal has a sinusoidal behavior, with annual and semi-annual harmonics. The spatial distribution of the correlation coefficient presented in Figure 2 unveils the fact that 98% of the stations have moderate to strong correlations between the LC phase RMS/A-RMS and PWV. When comparing the correlation coefficient between the PWV and LC phase RMS at 3° cutoff elevation and 10° cutoff elevation, 80% of the GNSS stations have a lower correlation coefficient for the first strategy, whereas in the case of A-RMS, the proportion remains the same. The stations that present the lowest correlation coefficient are located on Iceland, whereas the highest correlation is for the stations located in the central and south part of Finland.

We have averaged the phase residual RMS scatter for the results when using a cutoff elevation angle of 3° and the results when using a 10° cutoff elevation angle. By comparing each individual solution with the averaged solution of the RMS scatter, this becomes a useful measure for the phase modelling, and also for identifying the multipath effects on each individual GNSS station. Due to its general form, the multipath effect in GNSS causes periodic oscillations in the phase residuals, because of the change in path length between the direct and reflected signals [40,41]. Generally, the behavior of the phase residuals remains approximately constant over time, with the exception of when new, tall buildings are constructed, soil moisture effects [41], or when the growth of the natural vegetation occurs [27], which should be taken into account, especially when analyzing potential transient deformation signals, such that large multipath effects in general do not bias estimates of the GNSS stations displacements. Basically, if we use the same data and the same processing strategy each time for position estimation, then the multipath error will map into position estimates in the same manner each day.

When using the A-RMS, there is an improvement in the mean phase RMS scatter of 33% when using the 3° cutoff elevation angle, whereas in the case of using a 10° cutoff elevation angle, the improvement is 37%. During the summer months, the A-RMS can reduce the scatter with about 24% compared to the phase LC RMS.

From Figure 1, we see that there is not an evident cutback of the daily variability of the phase scatter by using the A-RMS for the 3° elevation angle processing strategy in

conjunction with the increase of the PWV, whereas in the case of the 10° elevation angle processing strategy, the A-RMS does not increase in conjunction with the increase in the PWV. Thus, the effect of the increase in the PWV on the 10° elevation angle processing strategy is strongly mitigated.

We have to keep in mind that a good performance of the LC phase RMS for GNSS stations is not the sole indicator and does not necessary imply a good positioning performance.

In Figure 12, the weighted average of daily position estimates for the North, East and Up components using the cutoff elevation angles of 3° and 10° is illustrated.
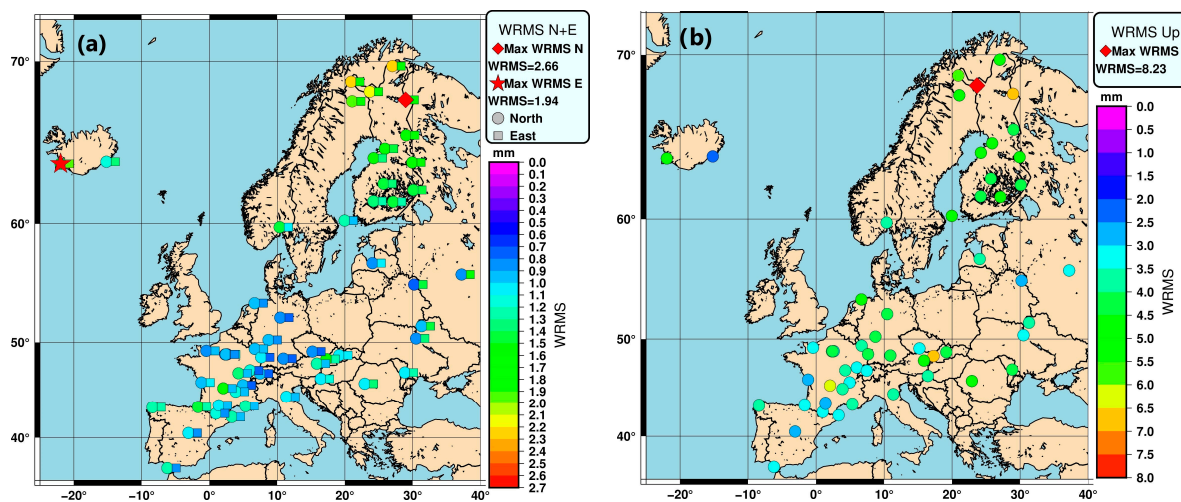
Figure 12. The weighted average of daily positions between the 3° cutoff elevation angle and 10° cutoff elevation angle for the (**a**) North, East position and (**b**) Up position.

We can notice that a high position scatter is present especially in the northern part of Scandinavia. In Appendix A, the weighted average of daily position estimates for the North, East and Up components is presented separately. The pattern of the WRMS scatter of the North component and its geographical distribution is similar to the East component according to Figures 7 and 8, and in conjunction with Figure 9 we can observe the correlation coefficient of 0.64 and 0.54 between the North and East WRMS scatters for all of the 55 GNSS stations when using the 10° cutoff elevation angle, respectively, with that of the 3° cutoff elevation angle. Also, the correlation between the GNSS station latitude and WRMS was assessed for all three position components according to Figure 11. The correlation for the cutoff elevation angle of 3° is as follows: (a) 0.60 for the North component, (b) 0.68 for the East component and (c) 0.47 for the Up component. For the latter, there is a moderate correlation, whereas for the horizontal component, there is a higher correlation coefficient for the East component compared to the North component. The correlation for the cutoff elevation angle of 10° is as follows: (a) 0.66 for the North component, (b) 0.76 for the East component and (c) 0.54 for the Up component. The results show a relatively higher correlation between the latitude and WRMS for the cutoff elevation angle of 10° as presented in Figure 11. One possibility for the increase in the WRMS scatter in the northern part of Europe can be attributed to the fact that in the processing strategy, no second order ionospheric effect was considered. This effect can be seen especially on the horizontal component, but on the Up component, we can also observe the extreme value of 8.23 mm, found in the northern part of Scandinavia. Also, the viscoelastic deformation effect of the solid Earth, due to the intraplate deformation, has to be accounted for in the increase in the WRMS for the Up component [27,42].

According to Figure 7 for the North component, more than 85% of the stations exhibit negative differences. This means that for the cutoff elevation angle of 10° we have a lower WRMS value when compared to the 3° cutoff elevation angle, which translates into a better repeatability for the results by using the strategy with a 10° cutoff elevation angle. A part

of the GNSS stations located in the northern part of Europe shows a better repeatability for the North component when using the strategy applying a 3° cutoff elevation angle, namely four GNSS stations out of seventeen—HETT, REYK, HOFN and SAVU—show an improvement in repeatability of around ~2%. From Figures 8 and 10, the East and Up components show that more than 78% of the GNSS stations have negative differences between employing a 10° cutoff elevation angle compared to a 3° cutoff elevation, thus when using a 10° cutoff elevation angle, we have better repeatability. A few of the GNSS stations, seven out of seventeen GNSS stations, located in the northern part of Europe show better repeatability for the East component when using the 3° cutoff elevation angle strategy, namely stations KUU2 and KIR0 show an improvement in repeatability of ~10%, whereas SAVU, ROM2, PYHA, KEV2 and HETT have an improvement in repeatability of around 2% to 4%. For the Up component, seven out of seventeen GNSS stations located in the upper part of Europe show a better repeatability when using a 3° cutoff elevation angle processing strategy such as ROM2, REYK and FINS, showing an improvement in repeatability of around 6%, while ORIV, OUL2, JOE2 and MIK3 show a 4% to 2% WRMS improvement.

From the histogram presented in Figure 5, when comparing the results by using the 3° elevation angle strategy (case (a)) and the 10° elevation angle processing strategy (case (b)), it is shown that for the North component, case (a) has a more conglomerated behavior around the values 2~3 mm, although in case (b), the WRMS has a more prominent spike for a higher number of stations with a repeatability of around 2~3 mm compared to case (a). For the East component, the WRMS in both cases is more similar compared to the North component, whereas for the Up component in case (a), we can observe that we have stations showing a WRMS of around 10~11 mm. For case (b), the WRMS is in the interval of 3~8 mm. Although there is not a statistically significant difference between the two strategies, we have identified, for the North and Up components in case (a), a few outliers.

In terms of repeatability, the difference in daily position estimates for the North component is 0.21 mm, and 0.16 mm for the East component, respectively, whereas for the Up component it presents a value of 0.75 mm. Overall, this indicates that the cutoff elevation angle has a relatively small impact using the two cutoff elevation angle processing strategies, which is confirmed also by the findings of [43,44] who used a cutoff elevation angle of 3°, 5°, 7°, 10°, 15° and 20° to study the repeatability of a daily static position. These results are based on a processing strategy that uses double difference, but another processing strategy is to use the precise point positioning technique (PPP). The dominant non-deterministic error source in daily GPS solutions is the common mode error (CME) [45,46]. The CME represents a sum of technique-dependent systematic errors and environmental effects that can generate important variations in a GPS time series [46,47].

Although the LC phase RMS for low elevation has weaker results compared to the 10° elevation angle, the low elevation observations are fundamental to decorrelate not only the station height, but also troposphere parameters and range biases. Thus, it is recommended, based on the results presented in the article, that we should conduct a thorough analysis not only on LC phase RMS, but also on station repeatability, especially on the day of the year when the maximum values occur, so that we are able to reduce the influence of different errors or, even better, mitigate that entire effect.

Applying a higher order ionospheric correction to the processing strategy to better evaluate the positional WRMS scatter could be a direction for further research, and this further research could also include the use of more GNSS stations that are in the northern and southern extremities of the Earth, and also in the equatorial area, which exhibits higher ionospheric scintillations. There are other very subtle effects that could have been omitted that could lead to incorrect assessments, such as the phase center offsets (PCO) for the latest satellites launched, errors that can lead to offsets and quasi-annual errors that can appear in the estimate of the time series position. Furthermore, there are errors which are harder to diagnose because of the repeating ground track and the routine orbital behavior of the satellites from a specific constellation, which manifest as annual signals, such as

the draconic period of the GPS satellite (with a ~351 days repeating period), which can be potentially reduced or eliminated through analogy with the results from other global navigation satellite constellations. This paper focuses solely on the processing of GPS data, and a combined solution with the solutions from other global constellations requires further research.

Appendix A

The weighted average of the daily position between the 3° cutoff elevation angle and 10° cutoff elevation angle for the North, East and Up positions.
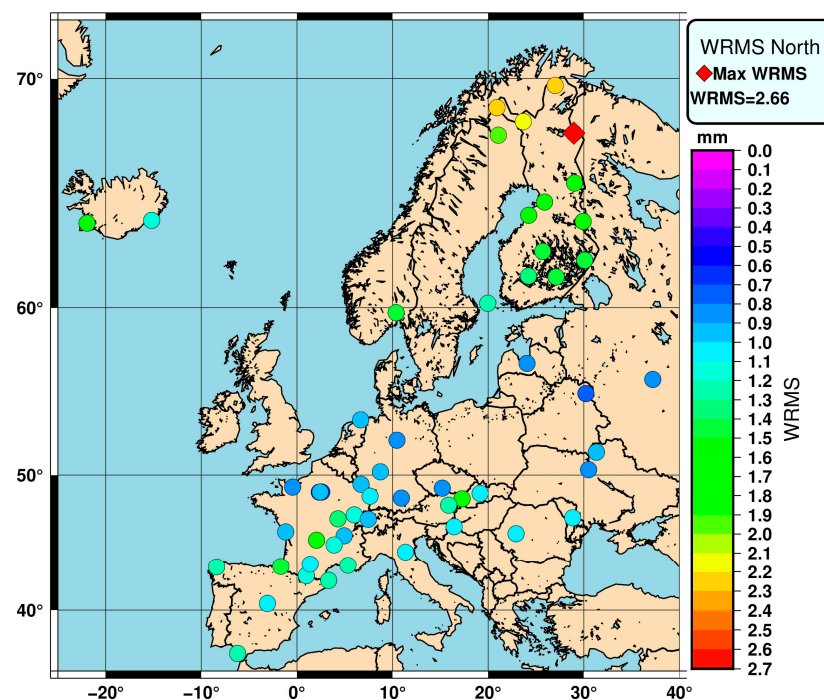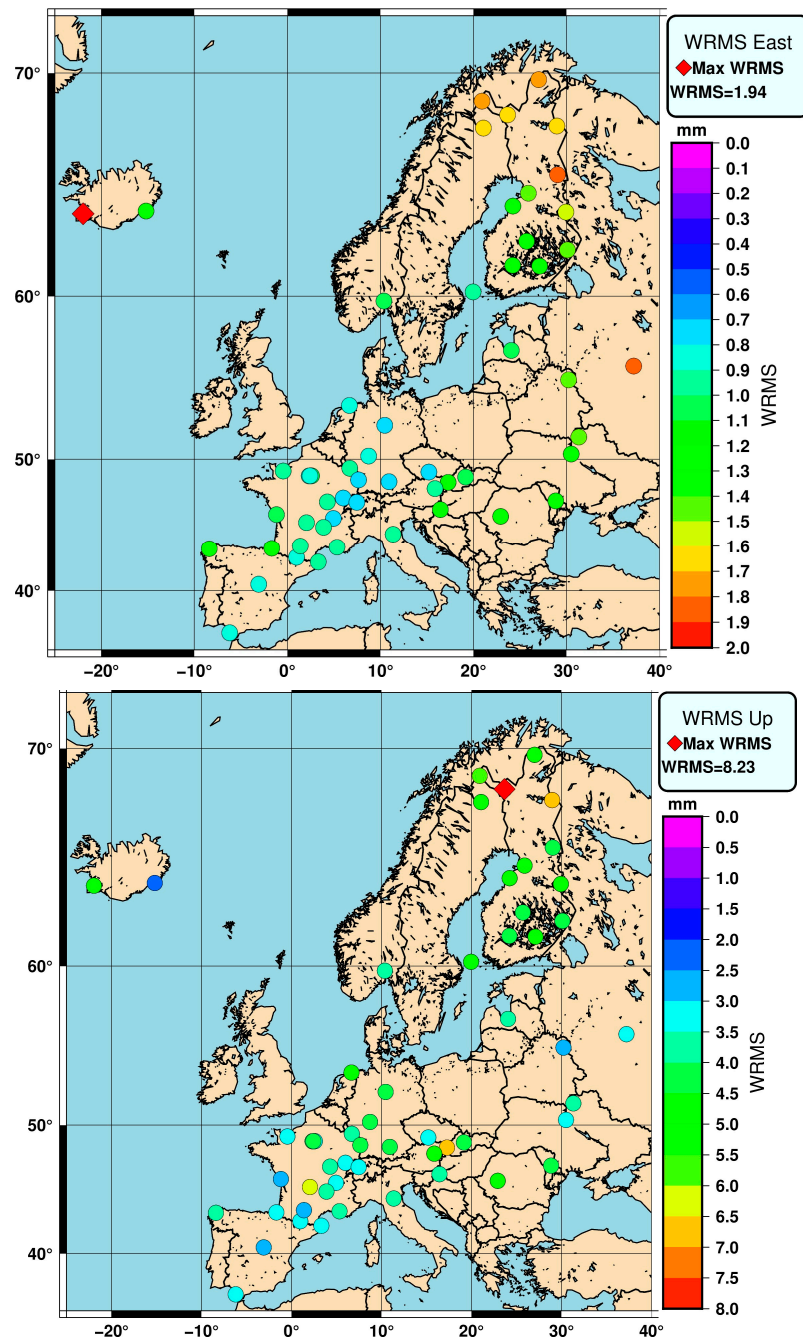

Figure A1. *Cont.*

Figure A1. The weighted average of daily positions between the 3° cutoff elevation angle and 10° cutoff elevation angle for the North, East and Up positions.

References

1. Vey, S.; Dietrich, R.; Fritsche, M.; Rülke, A.; Rothacher, M.; Steigenberger, P. Influence of mapping function parameters on global GPS network analyses: Comparisons between NMF and IMF. *Geophys. Res. Lett.* **2006**, *33*, L01814. [CrossRef]
2. Tesmer, V.; Boehm, J.; Heinkelmann, R.; Schuh, H. Effect of different tropospheric mapping functions on the TRF, CRF and position time-series estimated from VLBI. *J. Geod.* **2007**, *81*, 409–421. [CrossRef]
3. Nistor, S.; Suba, N.-S.; Buda, A.-S. The impact of tropospheric mapping function on PPP determination for one-month period. *Acta Geodyn. Geomater* **2020**, *17*, 237–252. [CrossRef]
4. Bahadur, B. An improved weighting strategy for tropospheric delay estimation with real-time single-frequency precise positioning. *Earth Sci. Inform.* **2022**, *15*, 1267–1284. [CrossRef]
5. Nistor, S.; Buda, A.S. Using Different Mapping Function In GPS Processing For Remote Sensing The Atmosphere. *J. Appl. Eng. Sci.* **2015**, *5*, 73. [CrossRef]

6. Stoew, B.; Nilsson, T.; Elgered, G.; Jarlemark, P.O.J. Temporal correlations of atmospheric mapping function errors in GPS estimation. *J. Geod.* **2007**, *81*, 311–323. [CrossRef]
7. Abdellaoui, H.; Zaourar, N.; Kahlouche, S. Contribution of permanent stations GPS data to estimate the water vapor content over Algeria. *Arab. J. Geosci.* **2019**, *12*, 81. [CrossRef]
8. de Oliveira, P.S.; Morel, L.; Fund, F.; Legros, R.; Monico, J.F.G.; Durand, S.; Durand, F. Modeling tropospheric wet delays with dense and sparse network configurations for PPP-RTK. *GPS Solut.* **2017**, *21*, 237–250. [CrossRef]
9. Ghoddousi-Fard, R.; Dare, P. A climatic based asymmetric mapping function using a dual radiosonde raytracing approach. In Proceedings of the 20th International Technical Meeting of the Satellite Division of the Institute of Navigation (ION GNSS 2007), Fort Worth, TX, USA, 25–28 September 2007; pp. 2870–2879.
10. Ghoddousi-Fard, R.; Dare, P.; Langley, R.B. Tropospheric delay gradients from numerical weather prediction models: Effects on GPS estimated parameters. *GPS Solut.* **2009**, *13*, 281–291. [CrossRef]
11. Zhang, D.; Guo, J.; Fang, T.; Wei, N.; Mei, W.; Zhou, L.; Yang, F.; Zhao, Y. TMF: A GNSS Tropospheric Mapping Function for the Asymmetrical Neutral Atmosphere. *Remote Sens.* **2021**, *13*, 2568. [CrossRef]
12. Montenbruck, O.; Steigenberger, P.; Villiger, A.; Rebischung, P. On the relation of GNSS phase center offsets and the terrestrial reference frame scale: A semi-analytical analysis. *J. Geod.* **2022**, *96*, 90. [CrossRef]
13. Kiliszek, D.; Kroszczyński, K.; Araszkiewicz, A. Analysis of Different Weighting Functions of Observations for GPS and Galileo Precise Point Positioning Performance. *Remote Sens.* **2022**, *14*, 2223. [CrossRef]
14. Li, B.; Lou, L.; Shen, Y. GNSS Elevation-Dependent Stochastic Modeling and Its Impacts on the Statistic Testing. *J. Surv. Eng.* **2016**, *142*, 04015012. [CrossRef]
15. Bona, P. Precision, Cross Correlation, and Time Correlation of GPS Phase and Code Observations. *GPS Solut.* **2000**, *4*, 3–13. [CrossRef]
16. Borko, A.; Even-Tzur, G. Stochastic model reliability in GNSS baseline solution. *J. Geod.* **2021**, *95*, 20. [CrossRef]
17. Eueler, H.-J.; Goad, C.C. On optimal filtering of GPS dual frequency observations without using orbit information. *Bull. Géodésique* **1991**, *65*, 130–143. [CrossRef]
18. Tiberius, C.C.J.M.; Kenselaar, F. Estimation of the stochastic model for gps code and phase observables. *Surv. Rev.* **2000**, *35*, 441–454. [CrossRef]
19. Gao, C.; Wu, F.; Chen, W.; Wang, W. An improved weight stochastic model in GPS Precise Point Positioning. In Proceedings of the 2011 International Conference on Transportation, Mechanical, and Electrical Engineering (TMEE), Changchun, China, 16–18 December 2011; pp. 629–632.
20. Kazmierski, K.; Hadas, T.; Sośnica, K. Weighting of Multi-GNSS Observations in Real-Time Precise Point Positioning. *Remote Sens.* **2018**, *10*, 84. [CrossRef]
21. Bertiger, W.; Bar-Sever, Y.; Dorsey, A.; Haines, B.; Harvey, N.; Hemberger, D.; Heflin, M.; Lu, W.; Miller, M.; Moore, A.W.; et al. GipsyX/RTGx, a new tool set for space geodetic operations and research. *Adv. Space Res.* **2020**, *66*, 469–489. [CrossRef]
22. Shi, C.; Zhao, Q.; Geng, J.; Lou, Y.; Ge, M.; Liu, J. Recent development of PANDA software in GNSS data processing. In Proceedings of the International Conference on Earth Observation Data Processing and Analysis (ICEODPA), Wuhan, China, 28–30 December 2008; pp. 558–566.
23. Dach, R.; Lutz, S.; Walser, P.; Fridez, P. (Eds.) Bernese GNSS Software Version 5.2. 2015. Available online: https://boris.unibe.ch/72297/ (accessed on 3 May 2024).
24. Herring, T.; King, R.; Floyd, M.; McClusky, S. *GAMIT Reference Manual GPS Analysis at MIT Release 10.7*; GAMIT/GLOBK; Department of Earth, Atmospheric and Planetary Sciences, Massachusetts Institute of Technology: Cambridge, MA, USA, 2020.
25. Nistor, S.; Suba, N.-S.; El-Mowafy, A.; Apollo, M.; Malkin, Z.; Nastase, E.I.; Kudrys, J.; Maciuk, K. Implication between Geophysical Events and the Variation of Seasonal Signal Determined in GNSS Position Time Series. *Remote Sens.* **2021**, *13*, 3478. [CrossRef]
26. Nistor, S.; Suba, N.-S.; Maciuk, K.; Kudrys, J.; Nastase, E.I.; Muntean, A. Analysis of Noise and Velocity in GNSS EPN-Repro 2 Time Series. *Remote Sens.* **2021**, *13*, 2783. [CrossRef]
27. Herring, T.A.; Melbourne, T.I.; Murray, M.H.; Floyd, M.A.; Szeliga, W.M.; King, R.W.; Phillips, D.A.; Puskas, C.M.; Santillan, M.; Wang, L. Plate Boundary Observatory and related networks: GPS data analysis methods and geodetic products. *Rev. Geophys.* **2016**, *54*, 759–808. [CrossRef]
28. Agnieszka, W.; Dawid, K. Modeling seasonal oscillations in GNSS time series with Complementary Ensemble Empirical Mode Decomposition. *GPS Solut.* **2022**, *26*, 101. [CrossRef]
29. Dong, D.-N.; Bock, Y. Global Positioning System Network analysis with phase ambiguity resolution applied to crustal deformation studies in California. *J. Geophys. Res. Solid Earth* **1989**, *94*, 3949–3966. [CrossRef]
30. Amiri-Simkooei, A.R.; Jazaeri, S.; Zangeneh-Nejad, F.; Asgari, J. Role of stochastic model on GPS integer ambiguity resolution success rate. *GPS Solut.* **2016**, *20*, 51–61. [CrossRef]
31. Amiri-Simkooei, A.R.; Teunissen, P.J.G.; Tiberius, C.C.J.M. Application of Least-Squares Variance Component Estimation to GPS Observables. *J. Surv. Eng.* **2009**, *135*, 149–160. [CrossRef]
32. Amiri-Simkooei, A.R.; Zangeneh-Nejad, F.; Asgari, J. Least-Squares Variance Component Estimation Applied to GPS Geometry-Based Observation Model. *J. Surv. Eng.* **2013**, *139*, 176–187. [CrossRef]
33. Larson, K.M.; Agnew, D.C. Application of the global positioning system to crustal deformation measurement: 1. Precision and accuracy. *J. Geophys. Res. Solid Earth* **1991**, *96*, 16547–16565. [CrossRef]

34. Saastamoinen, J. Atmospheric correction for the troposphere and stratosphere in radio ranging of satellites. In *The Use of Artificial Satellites for Geodesy (Geophysical Monograph 15)*; AGU: Washington, DC, USA, 1972; pp. 247–251.

35. Tregoning, P.; Herring, T.A. Impact of a priori zenith hydrostatic delay errors on GPS estimates of station heights and zenith total delays. *Geophys. Res. Lett.* **2006**, *33*, L23303. [CrossRef]

36. Evans, J.D. *Straightforward Statistics for the Behavioral Sciences*; Thomson Brooks/Cole Publishing Co: Belmont, CA, USA, 1996; p. xxii, 600.

37. Bos, M.S.; Fernandes, R.M.S.; Williams, S.D.P.; Bastos, L. Fast error analysis of continuous GNSS observations with missing data. *J. Geod.* **2013**, *87*, 351–360. [CrossRef]

38. Ning, T.; Elgered, G. Trends in the atmospheric water vapour estimated from GPS data for different elevation cutoff angles. *Atmos. Meas. Tech. Discuss.* **2018**, *2018*, 1–25. [CrossRef]

39. Tregoning, P.; Boers, R.; O'Brien, D.; Hendy, M. Accuracy of absolute precipitable water vapor estimates from GPS observations. *J. Geophys. Res. Atmos.* **1998**, *103*, 28701–28710. [CrossRef]

40. Herring, T.; Gu, C.; Nafi Toksöz, M.; Parol, J.; Al-Enezi, A.; Al-Jeri, F.; Al-Qazweeni, J.; Kamal, H.; Büyüköztürk, O. GPS Measured Response of a Tall Building due to a Distant Mw 7.3 Earthquake. *Seismol. Res. Lett.* **2018**, *90*, 149–159. [CrossRef]

41. Larson, K.M.; Gutmann, E.D.; Zavorotny, V.U.; Braun, J.J.; Williams, M.W.; Nievinski, F.G. Can we measure snow depth with GPS receivers? *Geophys. Res. Lett.* **2009**, *36*, L17502. [CrossRef]

42. Kierulf, H.P.; Steffen, H.; Barletta, V.R.; Lidberg, M.; Johansson, J.; Kristiansen, O.; Tarasov, L. A GNSS velocity field for geophysical applications in Fennoscandia. *J. Geodyn.* **2021**, *146*, 101845. [CrossRef]

43. Wang, J.; Liu, Z. Improving GNSS PPP accuracy through WVR PWV augmentation. *J. Geod.* **2019**, *93*, 1685–1705. [CrossRef]

44. Zhou, F.; Li, X.; Li, W.; Chen, W.; Dong, D.; Wickert, J.; Schuh, H. The Impact of Estimating High-Resolution Tropospheric Gradients on Multi-GNSS Precise Positioning. *Sensors* **2017**, *17*, 756. [CrossRef] [PubMed]

45. Zhang, J.; Bock, Y.; Johnson, H.; Fang, P.; Williams, S.; Genrich, J.; Wdowinski, S.; Behr, J. Southern California permanent GPS geodetic array: Error analysis of daily position estimates and site velocities. *J. Geophys. Res. Solid Earth* **1997**, *102*, 18035–18055. [CrossRef]

46. Dong, D.; Fang, P.; Bock, Y.; Webb, F.; Prawirodirdjo, L.; Kedar, S.; Jamason, P. Spatiotemporal filtering using principal component analysis and Karhunen-Loeve expansion approaches for regional GPS network analysis. *J. Geophys. Res. Solid Earth* **2006**, *111*, B03405. [CrossRef]

47. Serpelloni, E.; Faccenna, C.; Spada, G.; Dong, D.; Williams, S.D.P. Vertical GPS ground motion rates in the Euro-Mediterranean region: New evidence of velocity gradients at different spatial scales along the Nubia-Eurasia plate boundary. *J. Geophys. Res. Solid Earth* **2013**, *118*, 6003–6024. [CrossRef]

48. Wessel, P.; Luis, J.F.; Uieda, L.; Scharroo, R.; Wobbe, F.; Smith, W.H.F.; Tian, D. The Generic Mapping Tools Version 6. *Geochem. Geophys. Geosystems* **2019**, *20*, 5556–5564. [CrossRef]

49. Bruyninx, C.; Habrich, H.; Söhne, W.; Kenyeres, A.; Stangl, G.; Völksen, C. Enhancement of the EUREF Permanent Network Services and Products. In Proceedings of the Geodesy for Planet Earth, Buenos Aires, Argentina, 31 August–4 September 2009; pp. 27–34.

50. Johnston, G.; Riddell, A.; Hausler, G. The International GNSS Service. In *Springer Handbook of Global Navigation Satellite Systems*; Teunissen, P.J.G., Montenbruck, O., Eds.; Springer International Publishing: Cham, Switzerland, 2017; pp. 967–982.

51. Noll, C.E. The crustal dynamics data information system: A resource to support scientific analysis using space geodesy. *Adv. Space Res.* **2010**, *45*, 1421–1440. [CrossRef]